Measurements of Interfacial Curvatures of Bicontinuous Structure from Three-Dimensional Digital Images. 2. A Sectioning and Fitting Method

4 AUTHORS, INCLUDING:

Takeji Hashimoto
Kyoto University
517 PUBLICATIONS **17,172** CITATIONS

SEE PROFILE

Hiroshi Jinnai
Tohoku University
234 PUBLICATIONS **4,238** CITATIONS

SEE PROFILE

Measurements of Interfacial Curvatures of Bicontinuous Structure from Three-Dimensional Digital Images. 2. A Sectioning and Fitting Method

Yukihiro Nishikawa,[†,‡] Tsuyoshi Koga,[†,§] Takeji Hashimoto,[*,†,∥] and Hiroshi Jinnai[*,†,⊥]

Hashimoto Polymer Phasing Project, ERATO, Japan Science and Technology Corporation, and Department of Polymer Chemistry, Graduate School of Engineering, Kyoto University, Kyoto 606-8501, Japan

A *novel* method was developed to measure the local curvatures of phase-separating interface, i.e., the mean and Gaussian curvatures, from three-dimensional (3D) digital images of the bicontinuous domain structures formed during a phase-separation process via spinodal decomposition (SD). One of the aims of the study is to quantify the local geometry of the interface and its time evolution. Distributions of the interfacial curvatures were obtained by calculating the curvatures at many points on the interface. The applicability and precision of the method were critically tested using various model surfaces, e.g., spheres, cylinders, ellipsoids of revolution, and an infinite periodic minimal surface (IPMS), Schoen's gyroid. The method was then applied to the 3D interface developed via SD of a polymer blend. It was found that the interface of the polymer blend (i) was, for the most part, hyperbolic and (ii) had a considerably broader curvature distribution than that of Schoen's gyroid, though area-averaged curvatures obtained in our previous study had the same characteristics as IPMS.

1. Introduction

Bicontinuous structures, consisting of two nonintersecting channel networks in space, are commonly observed in nature. They are observed in binary mixtures of polymers[1] and simple fluids[2] as transient nonequilibrium structures, especially in the course of spinodal decomposition (SD). Similar types of bicontinuous structures are also found in block copolymers[3,4] and microemulsions[5,6] at thermal equilibrium. The bicontinuous microdomain structures of the block copolymers appear in a narrow range of composition.[7] In the microemulsions, ternary mixtures of oil, water, and surfactants form the bicontinuous monolayer of surfactants under a subtle balance of hydrophobic and hydrophilic interactions.

To characterize such bicontinuous structures in various systems, interfacial curvatures are important quantities to be explored, because they are related to a key physical factor of minimization of the interfacial free energy and hence of the structure formation during the phase separation. According to the differential geometry,[8] the local shape of the interface is characterized by the mean curvature, *H*, and Gaussian curvature, *K*. The former is a measure of the concavity of the interface, and the latter classifies the type of the interface, i.e., elliptic ($K > 0$), parabolic ($K = 0$), and hyperbolic ($K < 0$) surfaces. A sphere, a cylinder, and a horse saddle are, respectively, typical examples of the elliptic, parabolic, and hyperbolic surfaces.

In our previous paper,[9] a method to measure the area-averaged curvatures of the interface from three-dimensional (3D) digital images was presented. It involves measurement of areas of surfaces that are parallel to the interface as a function of a displacement from it (parallel surface method, PSM), as detailed elsewhere.[9] The PSM was applied to the interface of the bicontinuous structure ("bicontinuous interface") of a polymer mixture developed via SD in order to examine the geometrical characteristics of the interface. We found $\langle H \rangle = 0$ and $\langle K \rangle < 0$ for the bicontinuous structure with equal phase volumes, where $\langle i \rangle$ ($i = H$ or K) denotes the area-averaged value of i.[10] The result that the interface is hyperbolic and $\langle H \rangle$ is zero is intriguing, because the bicontinuous interface of the polymer mixture appears to have a surface geometry close to a group of surfaces called the "(infinite) periodic minimal surfaces (IPMS)". However, whether one of the minimal surfaces can really be a model for the bicontinuous interface of the polymer mixture is not clear from the knowledge of the area-averaged curvatures only. This is because the periodic minimal surface requires $H = 0$ everywhere on the interface. Thus, it is necessary to evaluate distribution of the interface curvatures. In the present study, a *novel* method, which we refer to as a

† Japan Science and Technology Corporation.

‡ Present address: Structural Biochemistry Laboratory, The Institute of Physical and Chemical Research (RIKEN), 1-1-1 Kouto, Mikaduki, Sayo, Hyogo 679-5148, Japan.

§ Present address: Department of Polymer Chemistry, Graduate School of Engineering, Kyoto University, Kyoto 606-8501, Japan.

∥ Kyoto University.

⊥ Present address: Department of Polymer Science and Engineering, Kyoto Institute of Technology, Matsugasaki, Kyoto 606-8585, Japan.

(1) Hashimoto, T. In *Materials Science and Technology*; Cahn, R. W., Haasen, P., Kramer, E. J., Eds.; *Structure and Properties of Polymers*; Thomas, E. L., Vol. Ed.; VCH: Weinheim, 1993; Vol. 12, p 251.

(2) Gunton, J. D.; San Miguel, M.; Sahni, P. S. *Phase Transition and Critical Phenomena*; Domb, C., Lebowitz, J. L., Eds.; Academic Press: New York, 1983; Vol. 8, p 269.

(3) Thomas, E. L.; Anderson, D. M.; Henkee, C. S.; Hoffman, D. *Nature* **1988**, *334*, 598. Hasegawa, H.; Tanaka, H.; Yamasaki, K.; Hashimoto, T. *Macromolecules* **1987**, 20, 1651.

(4) Jinnai, H.; Nishikawa, Y.; Spontak, R. J.; Smith, S. D.; Agard, D. A.; Hashimoto, T. *Phys. Rev. Lett.* **2000**, *84*, 518.

(5) Jahn, W.; Strey, R. *J. Phys. Chem.* **1988**, *92*, 2294.

(6) Chen, S. H.; Lee, D. D.; Chang, S. L. *J. Mol. Struct.* **1993**, *296*, 259.

(7) Hajduk, D. A.; Harper, P. E.; Gruner, S. M.; Honeker, C. C.; Kim, G.; Thomas, E. L.; Fetters, L. J. *Macromolecules* **1994**, *27*, 4063.

(8) Hilbert, D.; Cohn-Vossen, S. *Geometry and the Imagination*; Chelsea Publishers: New York, 1952.

(9) Nishikawa, Y.; Jinnai, H.; Koga, T.; Hashimoto, T.; Hyde, S. T. *Langmuir* **1998**, *14*, 1242.
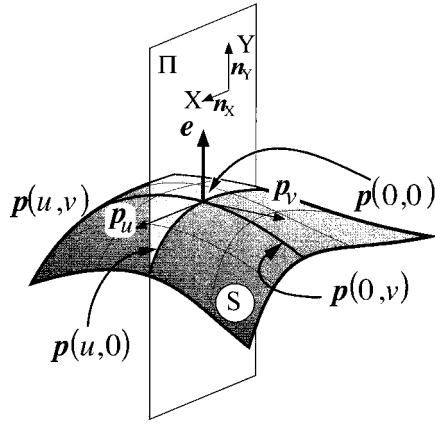
Figure 1. Schematic diagram of a surface, expressed in a parametric form $\mathbf{p}(u,v)$, and a "sectioning plane", Π, which define $\mathbf{p}(u,0)$. $\mathbf{p}(0,0)$ is a point of interest (POI) at which the local curvatures are measured. $\mathbf{e}$ is the unit normal vector of the surface at POI defined in the text. Note that the coordinate u and v have to be defined in such a manner that the vector $\mathbf{e}$ consistently points one of the two coexisting phases as described in section 3.2 in the text.

sectioning and fitting method (SFM), is proposed to determine the distribution of the local curvatures on the basis of the differential geometry.

2. Principle of the Sectioning and Fitting Method (SFM)

According to the differential geometry,[8] a surface is expressed in a parametric form as $\mathbf{p}(u,v) = (x(u,v), y(u,v), z(u,v))$, where $\mathbf{p}$ is a positional vector of the surface and u and v are curvilinear coordinates on the surface as shown in Figure 1. The definitions of u and v are arbitrary at this stage. The first and second fundamental forms of the differential geometry are defined, respectively, as[8]

$$\mathrm{I} = E\,\mathrm{d}u\,\mathrm{d}u + 2F\,\mathrm{d}u\,\mathrm{d}v + G\,\mathrm{d}v\,\mathrm{d}v \quad (1)$$

and

$$\mathrm{II} = L\,\mathrm{d}u\,\mathrm{d}u + 2\,M\,\mathrm{d}u\,\mathrm{d}v + N\,\mathrm{d}v\,\mathrm{d}v \quad (2)$$

The parameters in eqs 1 and 2 are given by

$$E = \mathbf{p}_u \cdot \mathbf{p}_u, \qquad F = \mathbf{p}_u \cdot \mathbf{p}_v, \qquad G = \mathbf{p}_v \cdot \mathbf{p}_v$$

$$L = \mathbf{p}_{uu} \cdot \mathbf{e}, \qquad M = \mathbf{p}_{uv} \cdot \mathbf{e}, \qquad N = \mathbf{p}_{vv} \cdot \mathbf{e} \quad (3)$$

The subscripts on $\mathbf{p}$ designate the partial derivatives, e.g., $\mathbf{p}_u \equiv \partial\mathbf{p}/\partial u$ and $\mathbf{p}_{uv} \equiv \partial^2\mathbf{p}/\partial u\,\partial v$. $\mathbf{e}$ is the unit vector normal to the surface at a point of interest (POI), calculated by the partial derivatives of $\mathbf{p}(u,v)$ from $\mathbf{e} = \mathbf{p}_u \times \mathbf{p}_v/|\mathbf{p}_u \times \mathbf{p}_v|$. Using these parameters, H and K are expressed as

$$H = \frac{EN + GL - 2FM}{2(EG - F^2)} \quad (4)$$

and

$$K = \frac{LN - M^2}{EG - F^2} \quad (5)$$

If the surface formula $\mathbf{p}(u,v)$ and its derivatives are known, H and K can be uniquely determined from eqs 3 to 5 at any points on the surface. However, in practice, it

is difficult to find out complete surface formula, $\mathbf{p}(u,v)$, in 3D space. Therefore, in the present study, we developed a scheme to evaluate curvatures without determining the complete surface formula, $\mathbf{p}(u,v)$.

Here, let POI be $\mathbf{p}(0,0)$. The surface is first "sectioned" by a plane including $\mathbf{p}(0,0)$ and $\mathbf{e}$. The intersection between the plane and the surface is defined as $\mathbf{p}(u,0)$. Parameters E and L in eq 3 are estimated from the partial derivatives of $\mathbf{p}(u,0)$ with respect to u at the POI. Subsequently, the surface is cut by another plane, also including $\mathbf{p}(0,0)$ and $\mathbf{e}$, that defines $\mathbf{p}(0,v)$. Now F, G, and N are estimated. The parameter M remains unsolved since the determination of complete functional form of the surface around $\mathbf{p}(0,0)$, i.e., $\mathbf{p}(u,v)$, involves two-dimensional fitting of the surface, accurate determination of which turned out to be technically very difficult. Thus, we rearranged eqs 4 and 5 to eliminate M:

$$4F_i^2\{L_iN_i - K(E_iG_i - F_i^2)\} - \\ \{E_iN_i + G_iL_i - 2H(E_iG_i - F_i^2)\}^2 = 0 \quad (6)$$

where the subscript i denotes ith set of the curvilinear coordinates (u,v) defined by two sectioning planes. The two unknown quantities, H and K, are invariant for any choice of the coordinates, while the other coefficients in eq 6 depend on the choice of the curvilinear coordinates, u and v. Therefore, eq 6 with two sets of the parameters $\{E_i, F_i, G_i, L_i, N_i\}$ obtained with two sets of (u,v) give the simultaneous equation for H and K.

3. Scheme of Measurement

3.1. Construction of 3D Interface. A 3D image is constructed from a stack of two-dimensional (2D) slices, i.e., a 3D array of image intensities. A similar kind of data format is often used for computer tomography (CT) and for magnetic resonance imaging (MRI), etc. as well as for laser scanning confocal microscopy (LSCM). The interface corresponds to a trajectory of the iso-intensity plane of a threshold value in the intensity distribution of the image. The Marching Cube Algorithm (MCA)[11] was used to model the interface. In this algorithm, a cube is created by eight pixels: four pixels from each of two adjacent slices. The vertexes of the cube locate at the center of each pixel. The image intensity at each pixel is assigned to the corresponding vertexes of the cube. If the intensity of one vertex of the edge is larger than the threshold value and if the intensity of another vertex of the same edge is smaller than the threshold value, this edge of the cube is considered to be intersected by the interface. The intersecting point of the interface at the edge of the cube is determined by a linear interpolation of the image intensity assigned to the two vertexes on the edge. By properly connecting the intersections, the interface is constructed and ultimately represented by a set of many triangles: Note that MCA defines the 14 types of intersection of the interface in the cube by taking the rotational and mirror symmetry into consideration.

3.2. Numerical Procedure of SFM. POI where the surface curvatures are measured was randomly selected among the vertexes of the triangles constructing the interface. To obtain H and K at POI based on the principle described in section 2, we first calculated intersections between the interface and the two sectioning planes at the POI, i.e., $\mathbf{p}(u,0)$ and $\mathbf{p}(0,v)$, as schematically shown in Figure 1. In order for the sectioning plane not to be tangential to the interface at POI, we force the sectioning

plane to include the unit vector corresponding to "the temporal normal", $\mathbf{e}'$, at the POI, which was estimated as an area average of the normal vectors of the triangles that shares the POI.

$$\mathbf{e}' = \sum_i A_\Delta^i \mathbf{e}_i / |\sum_i A_\Delta^i \mathbf{e}_i| \qquad (7)$$

Here $\mathbf{e}_i$ and A_Δ^i are, respectively, the normal vector and the area of ith triangle surrounding the POI. Note that $\mathbf{e}'$ is determined only from the coordinates of the vertexes of the triangles constructing the interface. Because the coordinates of the triangles are sometimes affected by noises in the raw LSCM 2D images, such as speckles, $\mathbf{e}'$ could be also affected by such noises. One of the advantages of SFM is that it does not rely on $\mathbf{e}'$, and the true normal, $\mathbf{e}$, can be independently found from $\mathbf{p}_u$ and $\mathbf{p}_v$, both determined by using the b-spline fitting as described below.

Let us define $X-Y$ coordinates characterized by unit vectors, $\mathbf{n}_X$ and $\mathbf{n}_Y$, which are in the sectioning plane, Π, as illustrated in Figure 1. Since the interface is constructed by many triangles, the intersection between the plane Π and the triangles (on the interface) forms a polygonal line, which is expressed in an array of the coordinates in the plane Π, $\{X_i, Y_i\}$ with $i = 0, 1, ..., $ typically up to 100. The POI is roughly at the middle of this array (i.e., typically $i \sim 50$). For the precise determination of the first- and second-order derivatives of the intersection at the POI, the polygonal line was first best-fitted with a smooth curve, for which we used the 4th order b-spline function.[12] To operate the fitting with the spline function, we chose a path length,

$$t_i \equiv \sum_{i=1}^{i} \sqrt{(X_i - X_{i-1})^2 + (Y_i - Y_{i-1})^2}$$

as a parameter because the length is a monotonically increasing variable. Thus, the fitting was performed for $\{t_i, X_i\}$ and $\{t_i, Y_i\}$,[12] from which a best-fitted functional form, $\{X(t), Y(t)\}$, was obtained. $\{X(t), Y(t)\}$ was then utilized to calculate $\mathbf{p}(u,0)$ through the following relation: $\mathbf{p}(u,0) = X(u)\mathbf{n}_X + Y(u)\mathbf{n}_Y$. The same protocol was repeated for the second intersection $\mathbf{p}(0,v)$. Note that u and v have to be defined in such a manner that the normal vector $\mathbf{e}$ at the POI consistently points to one of the subvolumes (divided by the interface) whose pixel intensity is larger than the threshold value.

The parameters in eq 6 (E, F, G, L, and N) were obtained from the derivatives of the two curvilinear coordinates determined by the two sectioning planes, $\mathbf{p}(u,0)$ and $\mathbf{p}(0,v)$. The two sets of the sectioning planes, in principle, give H and K. However, the resulting curvatures obtained by this scheme are, in practice, affected by (i) the precision of the b-spline fitting of the intersections between the interface and the sectioning plane and by (ii) the precision of F that is primarily determined by the angle between the two intersections. For example, in the special case where the intersections are perpendicular to each other (and hence $F = 0$), K cannot be obtained because the first term of the left-hand side of eq 6 including K becomes zero. Consequently, the results of H and K depend on the choice of the combination of the sectioning planes.

(10) Jinnai, H.; Koga, T.; Nishikawa, Y.; Hashimoto, T.; Hyde, S. T. *Phys. Rev. Lett.* **1997**, *78*, 2248. Jinnai, H.; Nishikawa, Y.; Morimoto, H.; Koga, T.; Hashimoto, T. *Langmuir*, **2000**, 16, 4380.
(11) Lorensen, W. E.; Cline, H. E. *Computer Graphics SIGGRAPH 87* **1987**, *21*, 163.
(12) de Boor, C. *A practical guide to splines*; Splinger-Verlag: New York, 1978.

Therefore, in our numerical scheme, we calculated curvatures at the POI as follows: (i) At first, 10 sets of the sectioning planes and then 10 sets of the parameters, $\{E_i, F_i, G_i, L_i, N_i\}$, are determined. (ii) The curvatures, H and K, are determined by nonlinear least-squares fitting on the basis of eq 6 by using these 10 sets of the parameters. (iii) Another pair of the sectioning planes and, hence, another set of the parameters, $\{E_i, F_i, G_i, L_i, N_i\}$, is further added to the initial 10 sets and the nonlinear least-squares fitting is again carried out in order to obtain the second trial function. (iv) Procedure (iii) was iterated until the convergence of an index, $\bar{\kappa} = (|\kappa_1| + |\kappa_2|)/2$, is attained. Here, κ_1 and κ_2 are the principal curvatures that are calculated from $H + \sqrt{H^2 - K}$ and $H - \sqrt{H^2 - K}$, respectively. The condition for the convergence of the index, $\bar{\kappa}$, is set as:

$$|\bar{\kappa}_{i+1} - \bar{\kappa}_i|/\bar{\kappa}_{i+1} < 1 \times 10^{-6} \qquad (8)$$

where $\bar{\kappa}_i$ is the index for the ith trial function. The criterion of 1×10^{-6} was determined from the series of precision tests using various model surfaces with known curvatures and curvature distributions (see section 4 for details). Rather than examining the convergence of H and K separately, the convergence of $\bar{\kappa}$ was considered for convenience, because it contains contributions from both H and K.

3.3. Statistical Analysis. Because the SFM provides the local curvatures of the interface, the measurements of them at many points on the interface give a joint probability density of H and K after the statistical treatment.

$$P(H,K) = \frac{1}{\Delta H \Delta K \sum_j \delta A(j)} \times$$
$$\sum_j \delta A\left(j \middle| H - \frac{\Delta H}{2} \le H(j) < H + \frac{\Delta H}{2} \text{ and } \right.$$
$$\left. K - \frac{\Delta K}{2} \le K(j) < K + \frac{\Delta K}{2}\right) \quad (9)$$

Here $H(j)$ and $K(j)$ are the mean and Gaussian curvatures at the jth POI. The term $\delta A(j|H - \Delta H/2 \cdots)$ denotes the area on which the jth POI satisfies its local curvatures given by $H - \Delta H/2 \le H(j) < H + \Delta H/2$ and $K - \Delta K/2 \le K(j) < K + \Delta K/2$. ΔH and ΔK are the class intervals of H and K. According to the definition of the joint probability density, the front factor $1/\Delta H \Delta K \sum_j \delta A(j)$ in eq 9 was introduced for the normalization condition, $\Sigma_H \Sigma_K P(H,K)\Delta H \Delta K = 1$, which can be replaced to $\int\int P(H,K)\, \mathrm{d}H\, \mathrm{d}K = 1$, if $\Delta H \to 0$ and $\Delta K \to 0$. The local area assigned to the jth point on the interface, $\delta A(j)$, was calculated as

$$\delta A(j) = \frac{1}{3}\sum_i A_\Delta^i(j) \qquad (10)$$

where $A_\Delta^i(j)$ is the area of ith triangle sharing the jth point. The factor 1/3 is necessary to avoid overcounting the total area for three times, since there are three vertexes in each triangle that can be POI. Similar to eq 9, marginal probability densities of the mean curvature, $P_H(H)$, and

that of the Gaussian curvature, $P_K(K)$, are also obtained from

$$P_H(H) =$$
$$\frac{1}{\Delta H \sum_j \delta A(j)} \sum_j \delta A\left(j \middle| H - \frac{\Delta H}{2} \le H(j) < H + \frac{\Delta H}{2}\right) \quad (11)$$

and

$$P_K(K) = \frac{1}{\Delta K \sum_j \delta A(j)} \sum_j \delta A\left(j \middle| K - \frac{\Delta K}{2} \le K(j) < K + \frac{\Delta K}{2}\right)$$
$$(12)$$

Normalization of $P_H(H)$ and $P_K(K)$ are $\sum P_H(H)\Delta H = \sum P_K(K)\Delta K = 1$ and $\int P_H(H)\,dH = \int P_K(K)\,dK = 1$ in the limit of $\Delta H \to 0$ and $\Delta K \to 0$, respectively. The area-averaged surface curvatures are also calculated as

$$\langle H \rangle = \frac{\sum_j \delta A(j) H(j)}{\sum_j \delta A(j)} \quad (13)$$

$$\langle K \rangle = \frac{\sum_j \delta A(j) K(j)}{\sum_j \delta A(j)} \quad (14)$$

The estimation for the statistical errors on $P_H(H)$ and $P_K(K)$ is described in Appendix C.

4. Application of SFM to Model Surfaces

4.1. Application of SFM to Elliptic and Parabolic Surfaces. The precision of the SFM was extensively tested for spheres and cylinders. They are, respectively, the simplest examples of the elliptic and parabolic surfaces. The 3D interfaces are generated from

$$f(x,y,z) = \sqrt{(x - x_0)^2 + (y - y_0)^2 + (z - z_0)^2} - r = 0$$
$$\text{(for spheres)} \quad (15)$$

and

$$f(x,y,z) = \sqrt{(x - x_0)^2 + (y - y_0)^2} - r = 0$$
$$\text{(for cylinders)} \quad (16)$$

Here (x_0, y_0, z_0) and (x_0, y_0) correspond to the center of a sphere and a cylinder, respectively, and r is the radius. The principal curvatures are $\kappa_1 = \kappa_2 = 1/r$ for the sphere and $\kappa_1 = 1/r$, $\kappa_2 = 0$ for the cylinder. The radius r was varied from 3.2 to 300 pixels for the spheres. The 3D surface of each object (either the sphere or cylinder) with a given radius r was represented by a set of triangles based on the MCA described earlier in section 3.1, and its principal curvatures were measured by the SFM described earlier in section 3.2.

Accuracy of the measurements depends strongly on the quality of the 3D surface. Roughness of a surface is quantified by an index, called "roughness index", RI,

$$\mathrm{RI} \equiv \sqrt{\langle A_\Delta \rangle} \frac{|\langle \kappa_1 \rangle| + |\langle \kappa_2 \rangle|}{2} \quad (17)$$
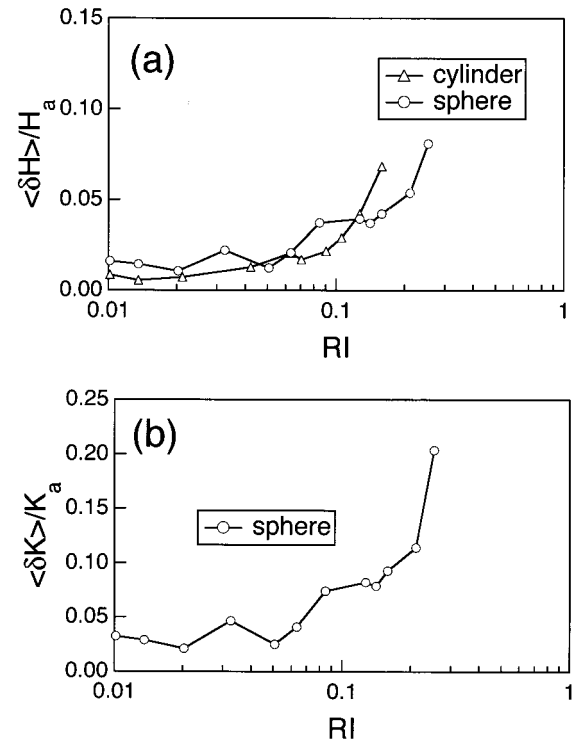

Figure 2. Relative discrepancies of (a) mean and (b) Gaussian curvature for cylinders and spheres estimated by SFM, which were plotted against roughness index, RI. The radii of spheres and cylinders, r, were varied from 3.2 to 300 pixels for spheres and from 2.5 to 300 pixels for cylinders, respectively. SFM results were averaged over 1000 points randomly selected on the surfaces.

where $\langle A_\Delta \rangle$ expresses an average area of each triangle, $\langle A_\Delta \rangle \equiv \Sigma_i A_\Delta^i/N_\Delta$, where N_Δ is the total number of triangles.[9] RI gives a measure of the roughness of the interface constructed by many triangles relative to the average radius of curvature. The smaller the value of RI, the smoother the surface becomes. RI ranged from 0.0027 to 0.25 for the spheres and from 0.0014 to 0.2 for the cylinders.

Figure 2 demonstrates the precision of the SFM measurements for spheres and cylinders, in which the relative discrepancies between the measured and analytical values of H and K are plotted against RI. The discrepancies were defined as follows:

$$\langle \delta H \rangle \equiv \sqrt{\langle (H_m - H_a)^2 \rangle}, \quad \langle \delta K \rangle \equiv \sqrt{\langle (K_m - K_a)^2 \rangle} \quad (18)$$

Here the subscripts m and a on the curvatures represent the measured and analytical values of the corresponding quantities, respectively. The analytical mean and Gaussian curvature, H_a and K_a, are given as $H_a = 1/r$ and $K_a = 1/r$ for the spheres and $H_a = 1/(2r)$ and $K_a = 0$ for the cylinders. In eq 18, $\langle \cdots \rangle$ denotes the average over number of data points. For the spheres and cylinders, for which the analytical values of curvatures do not have distributions, 1000 points on the surface were randomly selected for the SFM measurements. In Figure 2, $\langle \delta H \rangle$ and $\langle \delta K \rangle$ are normalized by their analytical values, i.e., $\langle \delta H \rangle/H_a$ and $\langle \delta K \rangle/K_a$. Note that $\langle \delta K \rangle/K_a$ was not plotted for the cylinders because $K_a = 0$. It was found both for the spheres and for the cylinders that $\langle \delta H \rangle/H_a$ increased with RI (Figure 2a). It seems that $\langle \delta H \rangle/H_a$ rapidly increases if RI exceeds 0.1. Similarly, $\langle \delta K \rangle/K_a$ also increased as RI increased. However, the relative magnitude of the discrepancy for the Gaussian curvature is larger than that

for the mean curvature; $\langle\delta K\rangle/K_a$ for spheres was about 10% at RI = 0.1, while $\langle\delta H\rangle/H_a$ for spheres was below 5% at the same RI. As for cylinders $\langle\delta H\rangle/H_a$ were not affected by the orientation of the surfaces, which was confirmed by changing the orientation of the cylinders with respect to the edge of the cube that contains cylinders.

4.2. Application of SFM to Ellipsoids of Revolution.
The most significant feature of the SFM is its ability to measure the distribution of the curvatures. The spheres and cylinders used in the previous section do not have such distributions: The probability density of curvatures for the simple surfaces is a delta function. Thus, the application of SFM to those simple interfaces offers a test of the "reliability" of the SFM measurement. If there were no error in SFM, it would always give the true single value and hence no error bars. Namely, the discrepancies estimated in Figure 2 demonstrate how the curvatures obtained from SFM deviate from the true analytical values.

We now apply SFM to another type of elliptic surface, ellipsoids of revolution, to check the ability of measuring distribution of curvatures as well as the precision of our method. For the model surface, curvatures depend on the position of the surface. The curvatures at each point of the surface as well as the curvature distribution can be numerically calculated on the basis of analytical formulas (see Appendix A for detail). The 3D surface of the object was calculated from the following equation:

$$f(x,y,z) = \sqrt{(x-x_0)^2 + (y-y_0)^2 + a^2(z-z_0)^2} - r = 0 \tag{19}$$

The aspect ratio of the radius, r/a, along the revolution axis (z-axis) to that, r, along the other axes (x- and y-axes) is given by $1/a$. Figures 3 and 4 together show a comparison of the probability densities of H and K estimated from both the SFM and the analytical method. The combination of the two parameters r and a determines not only RI but also H and K, and their distributions as well.

Parts a−c of Figure 3 demonstrate dependence of $\langle\delta H\rangle$ and $\langle\delta K\rangle$ (as shown by error bars in $H-K$ plane) on RI. The aspect ratio was kept constant in parts a−c ($1/a = 4$), while the radius r was changed from 18 to 7.6 pixels, corresponding to RI ranging from 0.04 to 0.10. The solid line represents the analytical result (according to the formulas in Appendix A) along which the data from the SFM should locate. It is shown for a given set of (H,K) that both $\langle\delta H\rangle$ and $\langle\delta K\rangle$ increased as RI increased (in the order of part a to part c). At a given r and a (or RI), the error bar increased as H or K increased. The dashed line shows the boundary condition, i.e., $K = H^2$: the condition $K \leq H^2$ is required for the two principal curvatures to be real numbers.

Parts b, d, and e of Figure 3 depict results for a given value of RI = 0.06 but different sets of r and a. The trajectory of H and K for each ellipsoid again follows the analytical result (solid line) but depends on the combination. As the aspect ratio, $1/a$, got larger (in the order part d, b, to e), the trajectory moved away from the $K = H^2$ line (dashed line) toward the axis of abscissa ($K = 0$) and the discrepancies $\langle\delta H\rangle$ and $\langle\delta K\rangle$ increased, especially, at large values of H and K. Overall, whatever the combination of r and a is, it seems that the measurements get less accurate as the curvatures locate away from the origin. The relative discrepancies, $\langle\delta H\rangle/H_a$ and $\langle\delta K\rangle/K_a$, for each ellipsoid together with RI are summarized in Table 1. Similar to the cases of spheres and cylinders, the relative discrepancies rapidly increase when RI exceeds 0.10.

Table 1. Error Estimation on the Ellipsoids of Revolution

r	a	RI	$\langle\delta H\rangle/H_a$	$\langle\delta K\rangle/K_a$
18	0.25	0.04	0.0088	0.006
12.3	0.25	0.06	0.011	0.093
7.6	0.25	0.11	0.033	0.22
13.1	0.5	0.06	0.011	0.042
12	0.14	0.06	0.011	0.018

Figure 4 demonstrates the SFM results on the probability densities $P_H(H)$ (part a) and $P_K(K)$ (part b) for a particular ellipsoid of revolution ($a = 0.25$, $r = 12.3$, RI = 0.06). The probability densities numerically calculated using equations given in Appendix A are shown as the solid line. Note that error bars in Figure 4 have a different meaning from those in Figure 3. Namely, $\langle\delta H\rangle$ and $\langle\delta K\rangle$ in Figure 3 demonstrate the difference between the measured curvatures at POI and those analytically obtained at the same POI, while the error bars presented in Figure 4 correspond to errors due to the statistical treatment in estimating the probability density (say "statistical error") as described further below. The statistical errors depend mainly on three factors, i.e., (i) the discrepancies in H and K, (ii) the error arising from the small amount of the sampling points, and (iii) the error related to the width of class intervals, ΔH and ΔK. Because the factors (ii) and (iii) are due to the statistical treatment, the more the sampling is made or the wider the class intervals become, the less the error bars on the probability densities become. The estimation of the statistical errors in the probability density is detailed in Appendix C.

There are no adjustable parameters involved in the calculation of the numerical probability densities in Figure 4 (solid line). Note that the ordinates in Figure 4 are logarithmic scales. The measured $P_H(H)$ and $P_K(K)$ *quantitatively* agreed over a range as large as 3 orders of magnitudes with the corresponding analytical results. The difference between the measured and analytical probability densities at the large curvatures is due to the shortage of the number of sampling points. This is because there are fewer amounts of vertexes on the model surface having the larger local curvatures compared with the surface having the smaller local curvatures.

4.3. Application of SFM to Hyperbolic Surfaces.
As an example of a hyperbolic surface, the surface given by $f(x,y,z) = z - xy = 0$ was chosen. This surface is displayed in Figure 5a and its surface curvatures are analytically given in Appendix B. A small portion of the hyperbolic surface ($|x| < 1.2$ and $|y| < 1.2$) was used for the precision check of the SFM. This portion of the hyperbolic surface is made in a cube with edge length composed of D pixels (D^3 pixel^3) as shown in Figure 5a. RI was varied by changing D, i.e., by adjusting the number of pixels expressing the same portion of the surface. For example, the hyperbolic surface with $D = 15.3$ pixel and that with $D = 5.0$ pixel correspond to RI = 0.035 and RI = 0.11, respectively.

Figures 5 and 6 together show a comparison of the curvature distributions measured by the SFM and those determined analytically. Figure 5b−d first show the reliability of SFM measurements for the three different RI. Data taken at various points on the hyperbolic surface are shown in the $H-K$ plane. $\langle\delta H\rangle$ and $\langle\delta K\rangle$ (defined earlier in eq 18) are plotted as error bars attached to the data. For a given value of RI, the error bars become larger as the measured points locate away from the origin in the $H-K$ plane. As RI increases in the order of b to d, the measured data spread over a larger area on the $H-K$ plane. The area appears to be triangular in shape for all
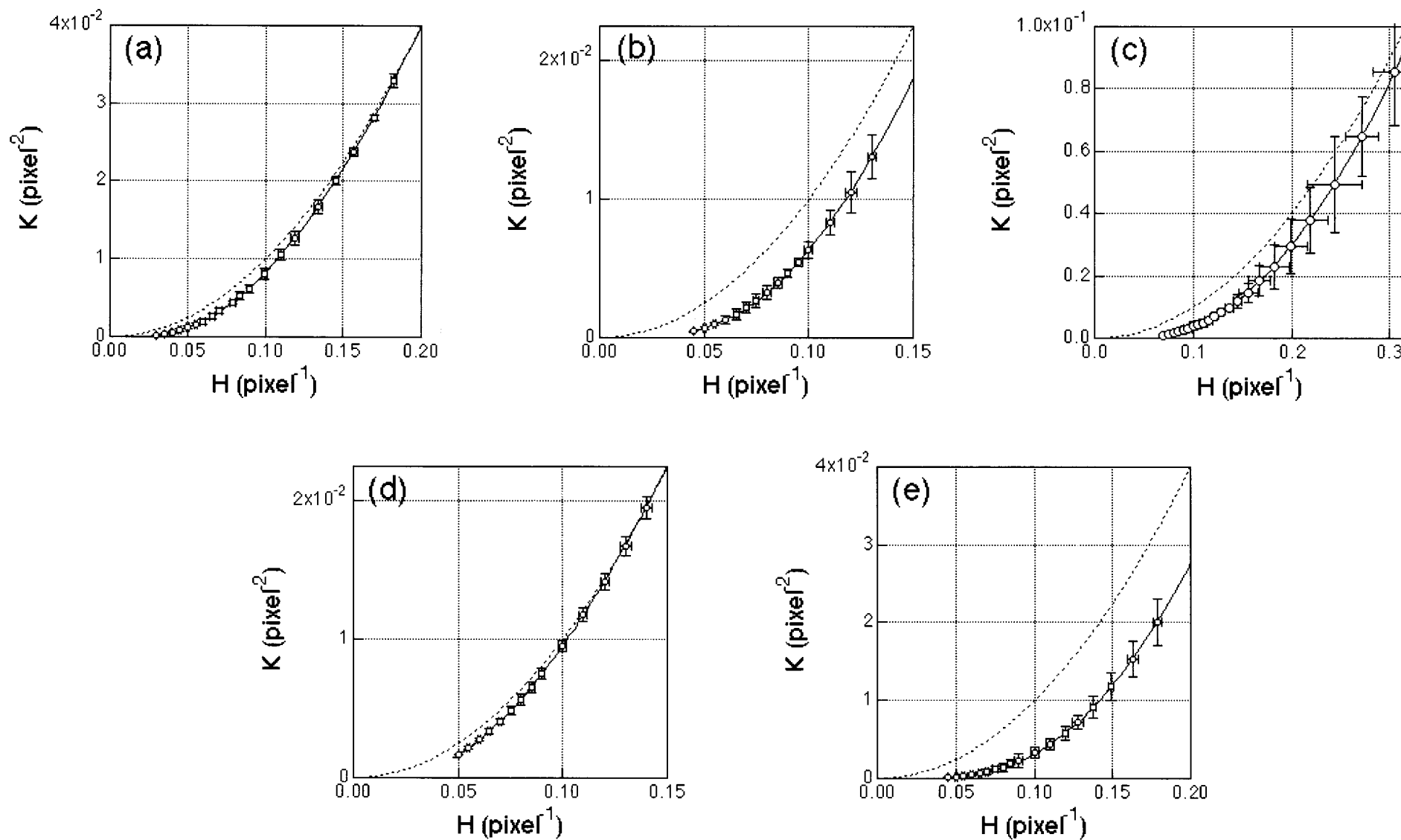
Figure 3. The curvatures estimated by SFM for ellipsoids of revolution. The parameters used were (a) $a = 0.25$ and $r = 18$, (b) $a = 0.25$ and $r = 12.3$, (c) $a = 0.25$ and $r = 7.6$, (d) $a = 0.5$ and $r = 13.1$, and (e) $a = 0.14$ and $r = 12$. Corresponding RI were (a) 0.04, (b) 0.06, (c) 0.10, (d) 0.06, and (e) 0.06, respectively. Solid lines are analytically evaluated surface curvatures. Region $K > H^2$ (the parameter space shown above the dashed line) is forbidden.
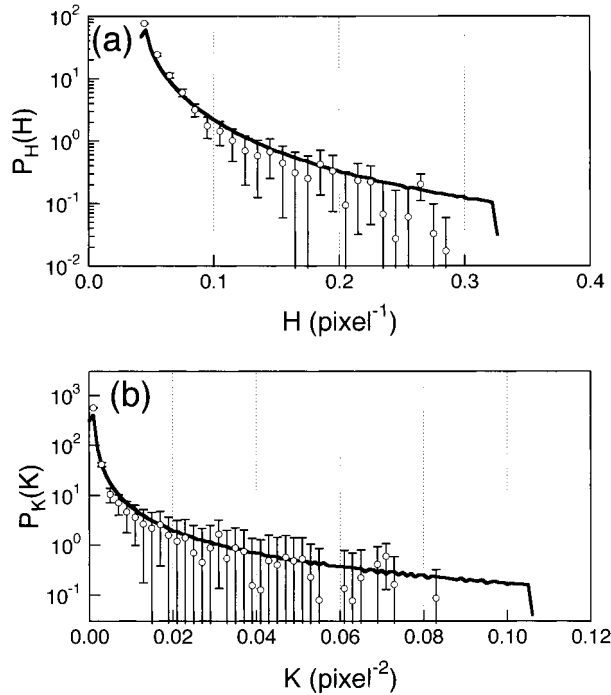
Figure 4. (a) $P_H(H)$ and (b) $P_K(K)$ for the ellipsoid of revolution with $a = 0.25$ and $r = 12.3$ (the same ellipsoid of revolution as that used in Figure 3b). The values obtained from SFM were plotted by symbol (○) with error bars calculated according to Appendix C. $P_H(H)$ and $P_K(K)$ analytically obtained as discussed in Appendix A were plotted by the solid lines.

Table 2. Error Estimation on the Gyroid

D	RI	$\langle\delta H\rangle/H_a$	$\langle\delta K\rangle/K_a$
15.3	0.035	0.12	0.058
7.8	0.06	0.12	0.12
5.0	0.11	0.15	0.18

hyperbolic surfaces. $\langle\delta H\rangle/H_a$ and $\langle\delta K\rangle/K_a$ were calculated at each POI and then averaged over the total number of measurements. The obtained results are summarized in Table 2. Note that the large values of $\langle\delta H\rangle/H_a$ and $\langle\delta K\rangle/K_a$ are due to the fact that the surface $z = xy$ includes a portion of $H_a \cong 0$ and/or $K_a \cong 0$ where the $\langle\delta H\rangle/H_a$ and $\langle\delta K\rangle/K_a$ become unexpectedly large. Just as in the case of the spheres and cylinders, these relative discrepancies rapidly increase when RI exceeds 0.15.

Figure 6 demonstrates the probability densities of the curvatures for $z = xy$ with $D = 46.2$ and RI = 0.01 (open circles).[13] $P_H(H)$ and $P_K(K)$ quantitatively agree with the numerically obtained probability densities (solid line). Note that there are no adjustable parameters involved in this comparison. Because of the restriction of the region, i.e., $|x| < 1.2$ and $|y| < 1.2$, the frequencies of the probability densities suddenly decreased at their edges. The agreement between the measured and the analytical probability densities is better than that for the ellipsoid (Figure 4). This difference is primarily due to the fact that RI of the hyperbolic surface is six times smaller than that of the ellipsoid. The smaller RI is, the better the accuracy for the probability densities.

4.4. Overall Precision of Measured H and K in $H-K$ Plane. As shown in the precision check of the SFM using the ellipsoid and the hyperbolic surface, the discrepancies strongly depend both on RI and on the combination of H and K, i.e., the location in the $H-K$ plane. Thus, to estimate the accuracy of the SFM measurements, it is necessary to have a 2D "discrepancy map" representing the extent of the discrepancies at a given set of curvatures and a

given RI. This map can directly be used to estimate statistical errors in the probability densities. Namely, one can estimate discrepancies δH and δK for a given set of H and K values from the map, and they are then used for further error calculations as described in Appendix C.

Figure 7 shows such an $H-K$ map that contains the discrepancies obtained in the preceding sections. This 2D map will be used for the error estimation of various surfaces having RI = 0.06. Needless to say, we can construct such 2D map for surfaces having other values of RI. The results of the ellipsoids of revolution for a given RI = 0.06 but with a various set of the radius and the aspect ratio are presented (diamonds with error bars). Similarly, discrepancies for the hyperbolic surface ($z = xy$) with RI = 0.06 (Figure 5c) are reproduced in Figure 7 (triangles with error bars). The circles and squares with error bars represent the results of spheres and cylinders for RI = 0.06, respectively. Thus, $\delta H(H,K)$ and $\delta K(H,K)$ are measured using four different types of model surfaces. Note that they are not continuous. Therefore, it is likely that a set of curvatures (H,K) in the SFM measurements cannot be found in the discrepancy map. In such cases, δH and δK of the data whose combination of curvatures (H,K) is closest to POI are used for the error estimation.

5. Application of SFM to 3D Interfaces

5.1. Application of SFM to a Model Bicontinuous Structure. We now apply the SFM to one of the infinite periodic minimal surfaces (IPMS), Schoen's gyroid.[14] In the present study, the gyroid is generated by using the trigonometric approximation:[15]

$$f(x,y,z) = \sin\frac{2\pi x}{L}\cos\frac{2\pi y}{L} + \sin\frac{2\pi y}{L}\cos\frac{2\pi z}{L} + \sin\frac{2\pi z}{L}\cos\frac{2\pi x}{L} \quad (20)$$

where L is the crystallographic unit cell length of the gyroid. The gyroid surface was generated in a cube (120 $\times$ 120 $\times$ 120 pixels^3)[16] in such a way that L was equal to 80 pixels. RI of the gyroid surface was 0.06. The probability densities of the gyroid measured with the SFM are presented in Figure 8. Error bars in $P_H(H)$ and $P_K(K)$ are estimated from the discrepancies determined using the model surfaces and presented in Figure 7. Nearly all (just under 100%) points locate in the $K < 0$ region (hyperbolic surface). It is intriguing that $P_K(K)$ showed a peak at around $K \cong -3.2 \times 10^{-3}$ pixel^{-2}. Figure 8 clearly shows that $P(H,K)$ distributes along $H = 0$, which is consistent with the definition of the periodic minimal surfaces. The obtained $P_H(H)$ by the SFM showed finite width, although it should be a delta function from the definition of IPMS, i.e., $H = 0$ everywhere on the surface. This is due to the facts that (i) we used the trigonometric approximation (eq 20) for generating the gyroid interface and (ii) SFM has some numerical discrepancies as discussed above. The area-averaged curvatures, $\langle H \rangle = 0$ pixel^{-1} and $\langle K \rangle = -2.4 \times 10^{-3}$ pixel^{-2}, calculated from the probability densities, were in excellent agreement with the analytical ones:[9] $\langle H_a \rangle = 0$ pixel^{-1} and $\langle K_a \rangle = -2.5 \times 10^{-3}$ pixel^{-2}. This

(13) Here we used the image of a hyperbolic surface, i.e., $z = xy$, at RI = 0.01 instead of that at RI = 0.06. This is because the hyperbolic surface having RI = 0.06 had too few vertexes, about 480, in the region used for the estimation of the discrepancies, i.e., $|x| < 1.2$, $|y| < 1.2$, to obtain enough statistical precision.

(14) Schoen A. H. NASA Technical Report No. 05541, 1970.

(15) Barnes, I. S.; Hyde, S. T.; Ninham, B. W. *J. Phys. (France) Colloq.* **1990**, supplement to 51, C7−19.

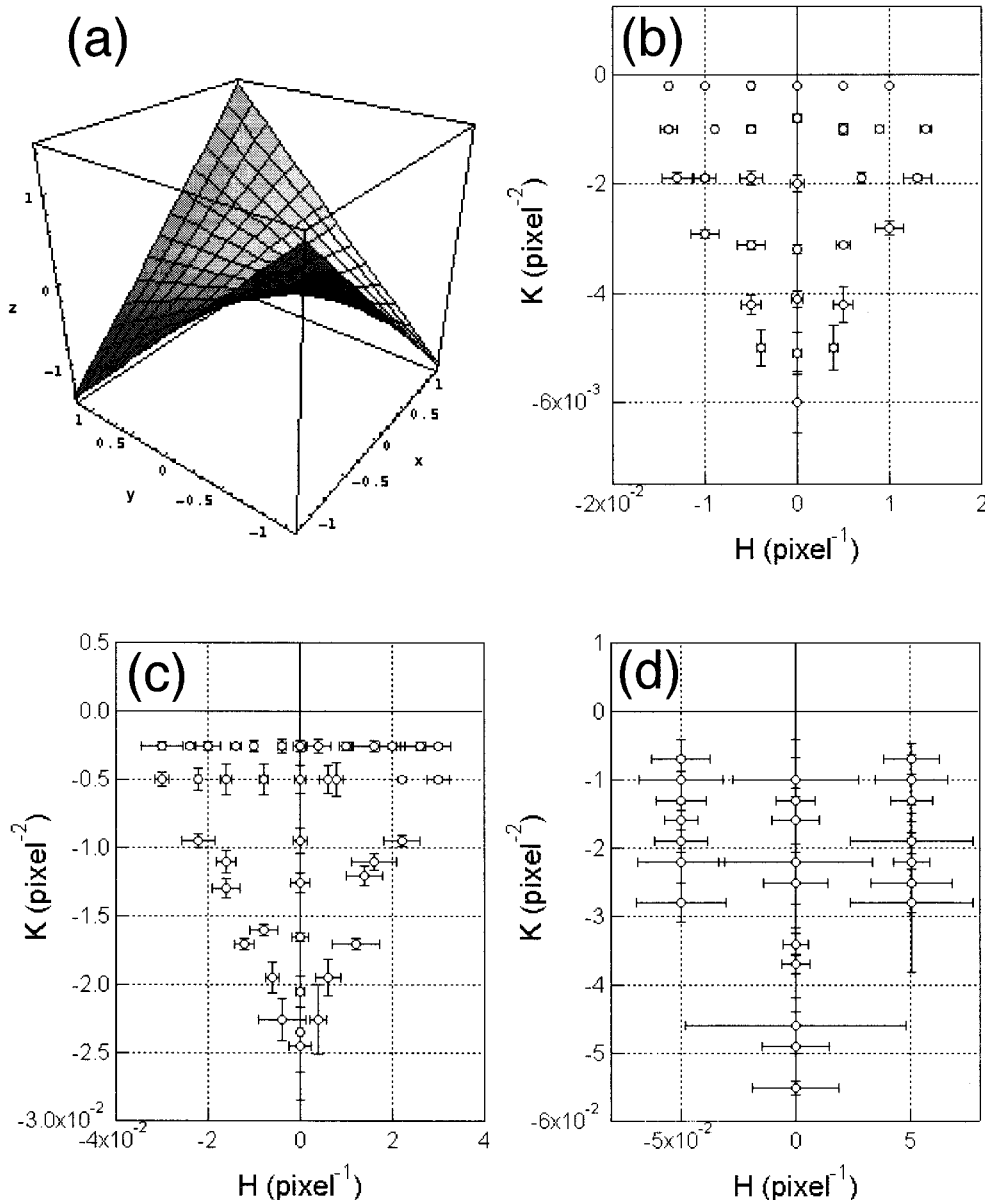(16) Corresponding 3D computer graphics was shown in Figure 5a of ref 9, for example.

Figure 5. (a) 3D representation of the hyperbolic surface given by $z = xy$ ($|x| < 1.2$, $|y| < 1.2$). Curvatures H and K as well as $\langle \delta H \rangle$ and $\langle \delta K \rangle$ measured at various points of the hyperbolic surface by SFM were plotted in b–d. $\langle \delta H \rangle$ and $\langle \delta K \rangle$ at each point in the H–K plane were indicated by error bars. Roughness index, RI, of the surface was varied by changing the number of pixels, D, comprising each triangle of the cube shown in a. (b) $D = 15.3$ (RI = 0.035), (c) $D = 7.8$ (RI = 0.06), and (d) $D = 5.0$ (RI = 0.11).

agreement suggests that the SFM is applicable to hyperbolic interfaces.

5.2. Application of SFM to a Bicontinuous Phase-Separated Structure of a Polymer Blend. We now employ SFM to a 3D interface of the bicontinuous phase-separated structure of a mixture of deuterated polybutadiene (DPB) and polybutadiene (PB) in the late stage of SD experimentally observed by LSCM.[10,17] The image was constructed by 110 optical slices of 512 pixel × 512 pixel two-dimensional images (0.2155 μm/pixel) which are 0.5 μm apart from each other along the incident laser beam direction. Part of the interface captured by LSCM is depicted in Figure 9. The experimental details can be found elsewhere.[10,17] The roughness index, RI, of the 3D interface was 0.06. A large number of points on the interface, 2×10^5, were randomly chosen from the many vertexes of triangles (ca. 2×10^6 points). The number of data points

(17) Jinnai, H.; Nishikawa, Y.; Hashimoto, T. *Phys. Rev. E* **1999**, *59*, R2554.

corresponds to about 10% of the total measurable points on the interface. As discussed in Appendix D, the amount of sampling was sufficiently large so that $P(H,K)$ is invariant with further sampling.

The joint probability densities $P(H,K)$ as well as $P_H(H)$ and $P_K(K)$ obtained from the 3D interface of the DPB/PB mixture are presented in parts a, b, and c in Figure 10, respectively. Note that the curvature is defined as positive, if the center of the osculating circle locates in the PB domain. The results show the following features of the interface. (i) $P_H(H)$ has a maximum at $H = 0$ and is symmetric around $H = 0$ so that $\langle H \rangle \cong 0$. (ii) Most of the measured points (up to 93%) locate in the $K < 0$ region. The feature (i) implies that the interface of the bicontinuous structure evolves with the least minimal energy path during the phase separation. The feature (ii) demonstrates that the interface formed by SD at the critical composition is hyperbolic at almost all points on the interface.
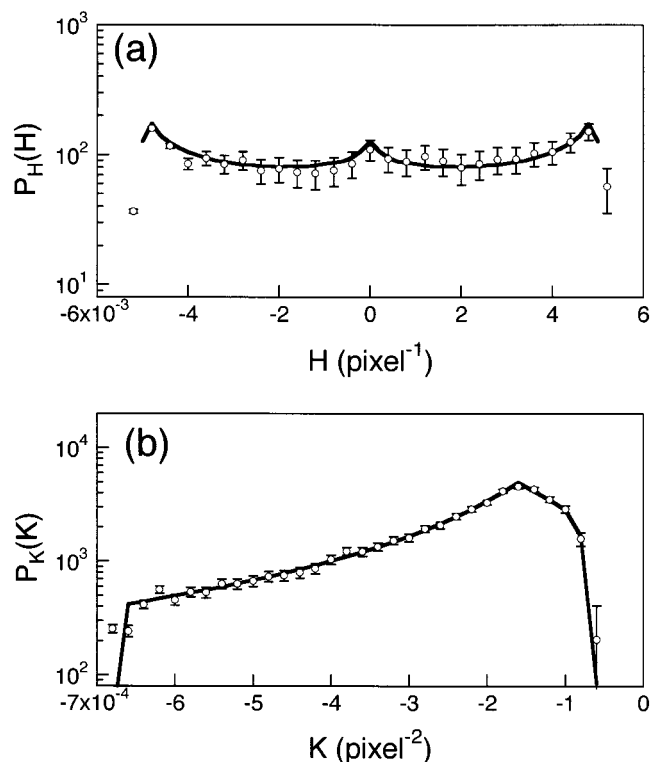
Figure 6. (a) $P_H(H)$ and (b) $P_K(K)$ for the hyperbolic surface, $z = xy$, with $D = 46.2$ pixels (RI = 0.01). The values obtained from SFM were plotted by open circles with error bars (calculated according to the method discussed in Appendix C). $P_H(H)$ and $P_K(K)$ analytically obtained as described in Appendix B were plotted by solid lines.
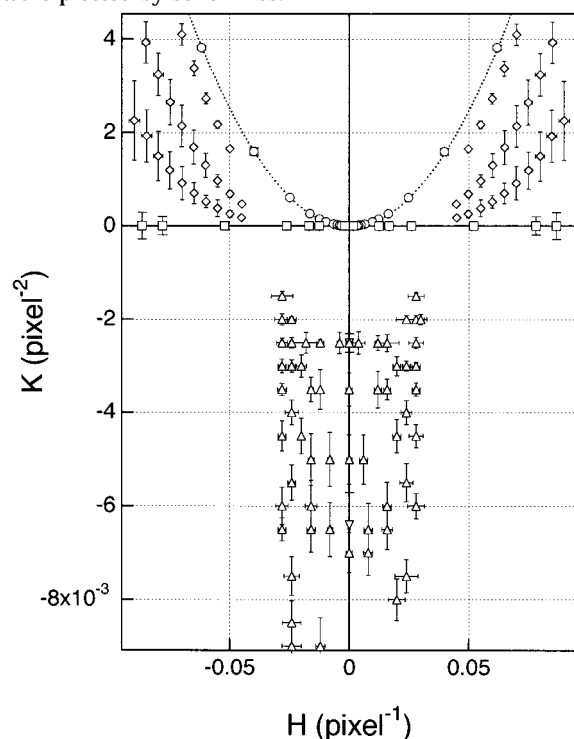

Figure 7. $H–K$ map summarizing the discrepancies between the curvatures obtained with the SFM method and those with the analytical methods for three types of surfaces, i.e., an elliptic, a parabolic, and a hyperbolic surface with a given RI of 0.06. The $K > H^2$ region partitioned by the dotted line is forbidden. The data plotted by the triangles and diamonds are, respectively, obtained from $z = xy$ and ellipsoids of revolution, while the data shown by circles and squares are from spheres and cylinders, respectively. Bars attached to each data point show the discrepancies.
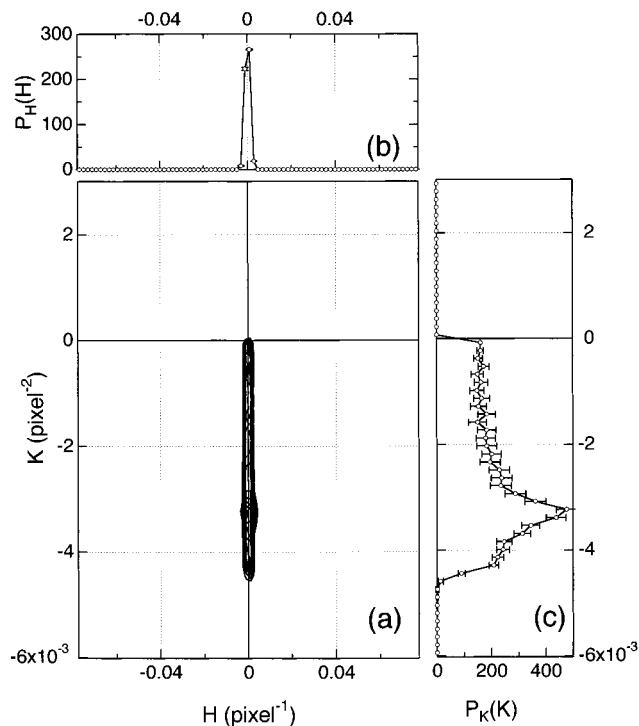

Figure 8. Probability densities of the surface curvatures of Schoen's gyroid. The contour map of the joint probability density, $P(H,K)$, is shown in part a. The marginal probability densities of mean, $P_H(H)$, and Gaussian curvatures, $P_K(K)$, are, respectively, plotted on the top (b) and the right (c).
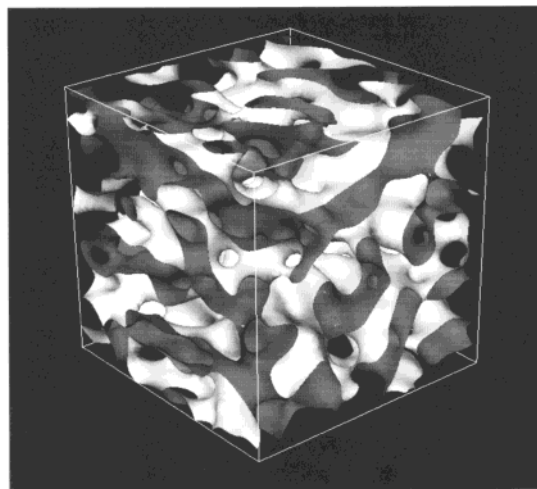

Figure 9. 3D reconstruction of interface of bicontinuous phase-separated structure of DPB/PB polymer blend observed by LSCM. The 3D interface was obtained at the reduced time $\tau = 117$ and had characteristic length $L = 11.5$ μm and divided the two phases with equal volume.[10] The volume shown in the figure is $25 \times 25 \times 25$ μm^3. The PB-rich and DPB-rich phases fill up the lighter and darker sides of the interface, respectively.

In our previous paper,[9] we developed another method to measure interface curvatures, a parallel surface method (PSM), which involves measurement of areas of parallel surfaces, surfaces parallel everywhere to the interface, as a function of displacement from it. Following the PSM, we obtained area-averaged curvatures for the DPB/PB polymer mixture: $\langle H \rangle = 0.0036$ pixel^{-1} = 0.017 μm^{-1} = $0.197L^{-1}$ and $\langle K \rangle = -0.0034$ pixel^{-2} = -0.076 μm^{-2} = $-10.1L^{-2}$. Here L represents wavelength of the dominant mode of the concentration fluctuations: $L \equiv 2\pi/q_m$ (q_m is the wavenumber at the maximum intensity of the 3D Fourier transform of density−density correlation function
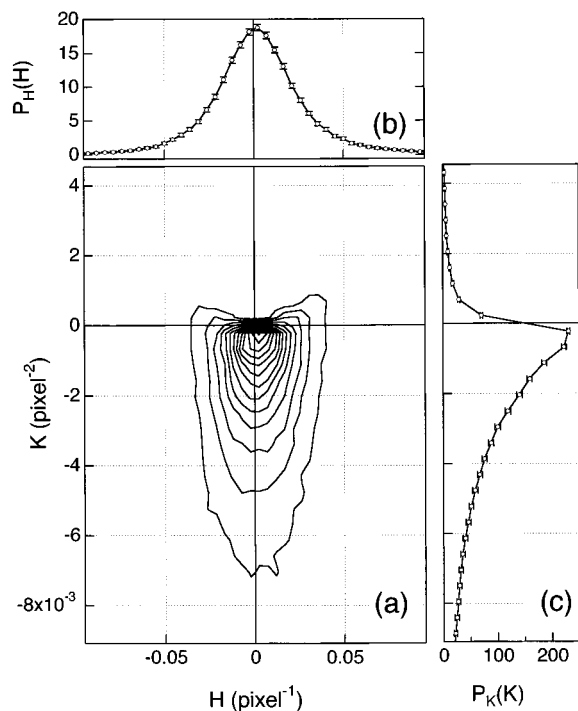
Figure 10. Probability densities of the interface curvatures of a 3D image of a polymer blend experimentally obtained by LSCM (see ref 10 for details). The joint probability density, $P(H,K)$, and the marginal probability densities, $P_H(H)$ and $P_K(K)$, were plotted in the same manner as in Figure 8. Note 0.2125 μm/pixel.

of the 3D image). The above results demonstrate that the interface, on average, consists of the hyperbolic surface. We emphasize here that the area-averaged mean and Gaussian curvatures obtained from the SFM ($\langle H \rangle = 0.010$ μm^{-1} and $\langle K \rangle = -0.080$ μm^{-2}) were in excellent agreement (within 3%) with those obtained from the PSM.

Now we can answer the question that we raised in the introductory part of the present paper, i.e., whether the interface of the bicontinuous polymer mixture developed in the nonequilibrium SD process resembles Schoen's gyroid? It is obvious from the comparison between Figures 8 and 10 that the probability density of the curvatures of the phase-separated polymer mixture differs from that of the gyroid, though the area-averaged quantities are similar. The polymer mixture has $P_H(H)$ much broader than that for the gyroid. It has $P_K(K)$ peaked in the vicinity of $K = 0$, while the gyroid has $P_K(K)$ peaked at a negative value of K.

Appendixes

A. Mean and Gaussian Curvatures of Ellipsoids of Revolution. Here we show analytical expression of the probability densities of the curvatures of the ellipsoids of revolution. The ellipsoid of revolution in eq 19 is expressed in a parametric form as

$$\mathbf{p}(u,v) = \begin{pmatrix} \cos(u)\cos(v) \\ \cos(u)\sin(v) \\ a^{-1}\sin(u) \end{pmatrix} \quad \text{(A1)}$$

where $0 \leq u \leq \pi$ and $0 \leq v \leq 2\pi$. According to eqs 3−5, the explicit forms of H and K can be obtained as

$$H(u,v) = \frac{1 + 3a^2 + (1 - a^2)\cos(2u)}{\sqrt{2}\{1 + a^2 + (1 - a^2)\cos(2u)\}^{3/2}} \quad \text{(A2)}$$

$$K(u,v) = \frac{4a^2}{\{1 + a^2 + (1 - a^2)\cos(2u)\}^2} \quad \text{(A3)}$$

Note that H and K depend only on u. The area element, $s(u,v)$, is calculated to be

$$s(u,v) = \sqrt{EG - F^2} =$$
$$\frac{\cos(u)}{\sqrt{2}a}\sqrt{1 + a^2 + (1 - a^2)\cos(2u)} \quad \text{(A4)}$$

The surface area, A, can be obtained from the following equation:

$$A = \int\int s(u,v)\,\mathrm{d}u\,\mathrm{d}v \quad \text{(A5)}$$

The coordinates (u,v) and $s(u,v)$ respectively correspond to j and δA in eqs 1 and 12. Therefore, the "true" values of $P_H(H)$ and $P_K(K)$ plotted in Figure 4 as solid lines were numerically calculated from eqs A2−A4 together with eqs 11 and 12, respectively.

B. Mean and Gaussian Curvatures of $z = xy$. H and K for $z = xy$ are analytically calculated as follows. The parametric form, $\mathbf{p}(u,v)$, of $z = xy$ becomes (u,v,uv). Its first and second derivatives are $\mathbf{p}_u = (1,0,v)$, $\mathbf{p}_v = (0,1,u)$, $\mathbf{p}_{uu} = (0,0,0)$, $\mathbf{p}_{uv} = (0,0,1)$, and $\mathbf{p}_{vv} = (0,0,0)$. The parameters in eq 3 thus become

$$E = 1 + v^2, \quad F = uv, \quad G = 1 + u^2, \quad L = N = 0,$$
$$\text{and } M = 1/\sqrt{1 + u^2 + v^2} \quad \text{(B1)}$$

where the normal vector $\mathbf{e}$ is

$$(-v,-u,1)/\sqrt{1 + u^2 + v^2}$$

According to eqs 3 to 5, H and K are calculated as

$$H(u,v) = \frac{-uv}{(1 + u^2 + v^2)^{3/2}} \quad \text{and}$$

$$K(u,v) = \frac{-1}{(1 + u^2 + v^2)^2} \quad \text{(B2)}$$

Note that K is always negative for all (u,v). The surface area element can be calculated in the same way as eq A4

$$s(u,v) = \sqrt{EG - F^2} = \sqrt{1 + u^2 + v^2} \quad \text{(B3)}$$

The true values of the probability densities shown in Figure 6 were obtained from numerical calculations based on the above equations given by eqs B2 and B3.

C. Statistical Errors on the Probability Densities. The estimation of the statistical errors on the probability densities was carried out according to statistical mathematics. Here we consider mean curvature, H, only, but the scheme is available for Gaussian curvature as well. Assuming the discrepancies in H measured by SFM obey the Gaussian distribution, the probability density, $Q_H(H;j)$, having H at a single POI (designated j) where the analytical mean and Gaussian curvatures are H_j and K_j,
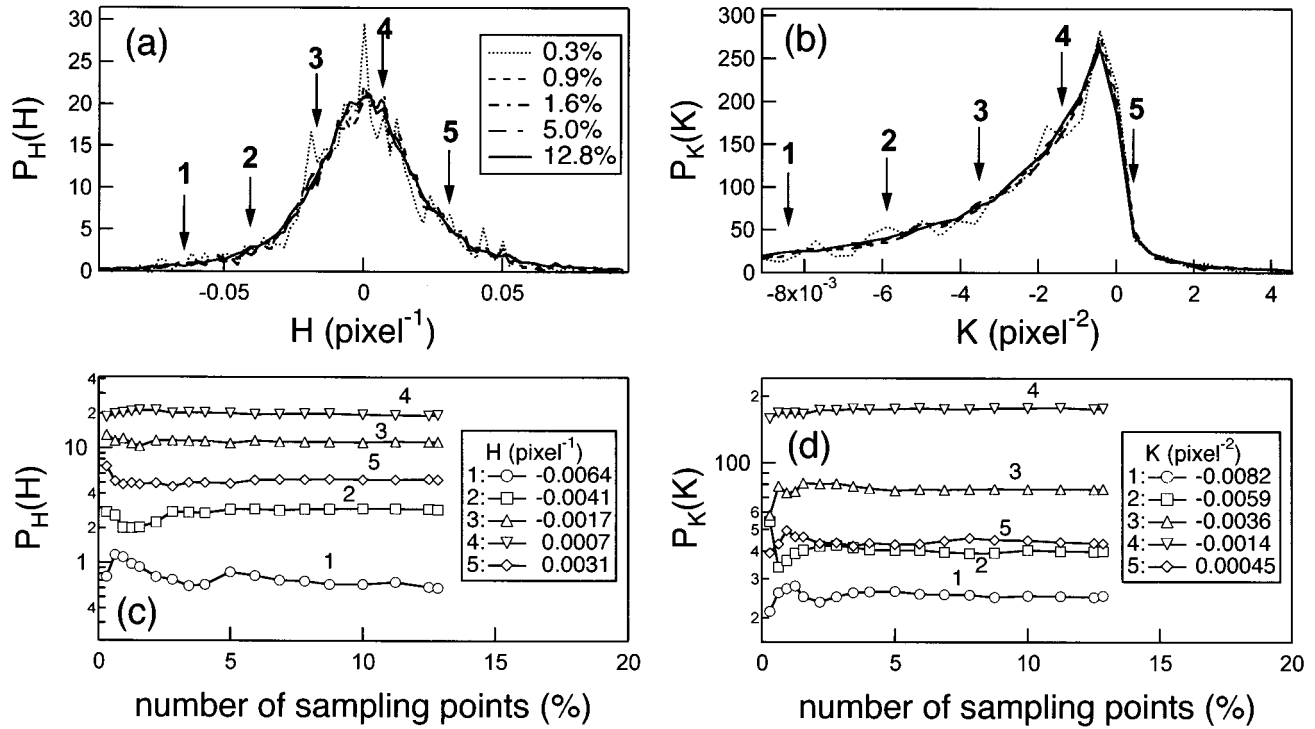
Figure 11. Effect of number of sampling points on convergence of probability density distributions, $P_H(H)$ (part a) and $P_K(K)$ (part b). The fluctuations of the marginal probability densities at the representative mean and Gaussian curvatures with number of sampling points were also shown in parts c and d, respectively. The representative mean and Gaussian curvatures used in parts c and d were, respectively, indicated by arrows with numbers in parts a and b.

respectively, is given by

$$Q_H(H;j) = \frac{1}{\sqrt{2\pi}\delta H(H_j,K_j)} \exp\left[-\frac{(H-H_j)^2}{2\{\delta H(H_j,K_j)\}^2}\right] \quad (C1)$$

where $\delta H(H_j,K_j)$ is the discrepancy of H at the jth POI having curvatures H_j and K_j. For the sake of convenience in the following discussion, we introduced another distribution function for at the jth POI, $G_H(H;j)$, which is defined as the integrated probability density of $Q_H(H;j)$.

$$G_H(H;j) \equiv \int_{-\infty}^{H} Q_H(H;j) \, dH \quad (C2)$$

$G_H(H;j)$ is the probability that the measured value of H at the jth POI would be less than H. The distribution function, $F_H(H)$, can be defined as the average of $G_H(H;j)$ over n points of interest

$$F_H(H) \equiv \frac{\sum_{j=1}^{n} \delta A(j) G_H(H;j)}{\sum_{j=1}^{n} \delta A(j)} \quad (C3)$$

where the area-weighting of the jth POI, $\delta A(j)$, is taken into account. The variance of $F_H(H)$, $V_H(H)$, is calculated as

$$V_H(H) = \frac{\sum_{j=1}^{n} \delta A(j) G_H(H;j)^2}{\sum_{j=1}^{n} \delta A(j)} - \{F_H(H)\}^2 \quad (C4)$$

$\sqrt{V_H(H)}$ is considered to be the statistical error on $F_H(H)$. Here we define

$$F_H^{(\pm)}(H) \equiv F_H(H) \pm \sqrt{V_H(H)} \quad (C5)$$

The probability density, $P_H(H)$, is defined as the derivative of $F_H(H)$

$$P_H(H) \equiv \frac{d}{dH} F_H(H) \quad (C6)$$

$$\cong \frac{1}{\Delta H}\left\{F_H\left(H+\frac{\Delta H}{2}\right) - F_H\left(H-\frac{\Delta H}{2}\right)\right\} \quad (C7)$$

Using C5, the upper and lower limits of $P_H(H)$, i.e., $P_H^+(H)$ and $P_H^-(H)$, respectively, can be calculated

$$P_H^{(\pm)}(H) \equiv \frac{1}{\Delta H}\left\{F_H^{(\pm)}\left(H+\frac{\Delta H}{2}\right) - F_H^{(\mp)}\left(H-\frac{\Delta H}{2}\right)\right\}$$

$$= P_H(H) \pm \frac{1}{\Delta H}\left\{\sqrt{V_H\left(H+\frac{\Delta H}{2}\right)} + \sqrt{V_H\left(H-\frac{\Delta H}{2}\right)}\right\} \quad (C8)$$

Thus, the statistical error on $P_H(H)$, $P_H^{err}(H)$, becomes

$$P_H^{err}(H) = \frac{1}{\Delta H}\left\{\sqrt{V_H\left(H+\frac{\Delta H}{2}\right)} + \sqrt{V_H\left(H-\frac{\Delta H}{2}\right)}\right\} \quad (C9)$$

D. Statistical Convergence of Probability Densities. The convergence of the probability densities of H and K were examined by varying the number of sampling points in the DPB/PB polymer mixture. Figures 11a and 11b demonstrate the $P_H(H)$ and $P_K(K)$ for various number

of sampling points. Note that the number of the sampling points are expressed as a percentage of the number of sampled vertexes of the triangles, which construct the surface, among the total number of vertexes. The fluctuation of the marginal probability densities of H and K converges into the smooth curves with an increase in the number of sampling points. In parts c and d, $P_H(H)$ and $P_K(K)$ at some representative H and K shown by arrows in parts a and b are plotted against the number of sampling points. In Figures 11c and 11d, $P_H(H)$ and $P_K(K)$ reached plateau values at all representative curvatures, if the number of the sampling points becomes larger than 10% of the total number of vertexes of the triangles.